Optimizing Interface Conductivity in Electronics

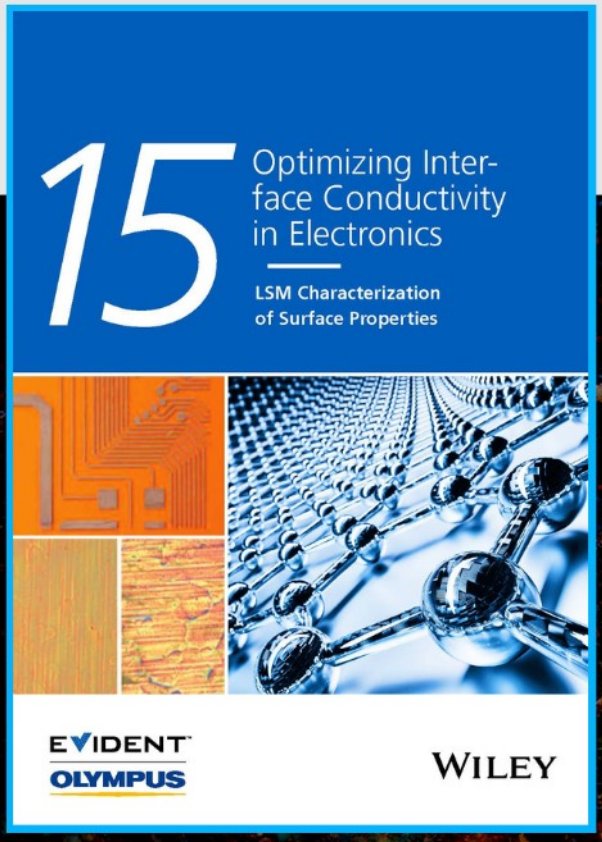

The latest eBook from Advanced Optical Metrology. Download for free.

Surface roughness is a key parameter for judging the performance of a given material's surface quality for its electronic application. A powerful tool to measure surface roughness is 3D laser scanning confocal microscopy (LSM), which will allow you to assess roughness and compare production and finishing methods, and improve these methods based on mathematical models.

Focus on creating high-conductivity electronic devices with minimal power loss using laser scanning microscopy is an effective tool to discern a variety of roughness parameters.

EVIDENT
OLYMPUS

WILEY

ADVANCED FUNCTIONAL MATERIALS
www.afm-journal.de

Modular Assembly of Red Blood Cell Superstructures from Metal–Organic Framework Nanoparticle-Based Building Blocks

Jimin Guo, Yunlong Yu, Wei Zhu, Rita E. Serda, Stefan Franco, Lu Wang, Qi Lei, Jacob Ongudi Agola, Achraf Noureddine, Evelyn Ploetz, Stefan Wuttke,* and C. Jeffrey Brinker**

Bio/artificial hybrid nanosystems based on biological matter and synthetic nanoparticles (NPs) remain a holy grail of materials science. Herein, inspired by the well-defined metal–organic framework (MOF) with diverse chemical diversities, the concept of "armored red blood cells" (armored RBCs) is introduced, which are native RBCs assembled within and protected by a functional exoskeleton of interlinked MOF NPs. Exoskeletons are generated within seconds through MOF NP interlocking based on metal-phenolic coordination and RBC membrane/NP complexation via hydrogen-bonding interactions at the cellular interface. Armored RBC formation is shown to be generalizable to many classes of MOF NPs or any NPs that can be coated by MOF. Moreover, it is found that armored RBCs preserve the original properties of RBCs (such as oxygen carrier capability and good ex ovo/in vivo circulation property) and show enhanced resistance against external stressors (like osmotic pressure, detergent, toxic NPs, and freezing conditions). By modifying the physicochemical properties of MOF NPs, armored RBCs provide the capability for blood nitric oxide sensing or multimodal imaging. The synthesis of armored RBCs is straightforward, reliable, and reversible and hence, represent a new class of hybrid biomaterials with a broad range of functionalities.

1. Introduction

Red blood cells (RBCs; also called erythrocytes),[1] the most abundant cellular constituent of blood, play a pivotal role in life processes such as the delivery of oxygen (O_2) to body tissues, the transfusion of medicine to different organs, and the regulation of the adaptive immune system. Due to their biocompatibility, abundance, and longevity in circulation, RBCs have been greatly explored as carriers of various compounds and nanoparticles. RBCs have served as an inspirational source of novel functional assemblies and advanced architectures for biomedical applications.[2] Examples range from coupling drugs onto the RBC surface to improve their delivery and therapeutic effects,[3] to the attachment of nanoparticles (NPs) onto the RBC membrane to alter their circulation behaviors,[4] to the encapsulation of RBCs with nanometric films to modulate immune

Dr. J. Guo, Dr. J. O. Agola, Dr. A. Noureddine, Prof. C. J. Brinker
Center for Micro-Engineered Materials and the Department of Chemical and Biological Engineering
The University of New Mexico
Albuquerque, NM 87131, USA
E-mail: jbrinker@unm.edu

Dr. J. Guo, Dr. R. E. Serda, S. Franco
Department of Internal Medicine
Molecular Medicine
The University of New Mexico
Albuquerque, NM 8713, USA

Prof. Y. Yu
National Engineering Research Center for Biomaterials
Sichuan University
Chengdu 610064, P. R. China

The ORCID identification number(s) for the author(s) of this article can be found under https://doi.org/10.1002/adfm.202005935.

DOI: 10.1002/adfm.202005935

Prof. W. Zhu, Dr. Q. Lei
MOE International Joint Research Laboratory on Synthetic Biology and Medicines
School of Biology and Biological Engineering
South China University of Technology
Guangzhou 510006, P. R. China
E-mail: zhuwei86@scut.edu.cn

Dr. L. Wang
Department of Biochemistry and Molecular Biology
University of New Mexico
Albuquerque, NM 87131, USA

Dr. E. Ploetz, Prof. S. Wuttke
Department of Chemistry and Center for NanoScience (CeNS)
University of Munich (LMU)
Butenandtstraße 11, Munich 81377, Germany
E-mail: stefan.wuttke@bcmaterials.net

Prof. S. Wuttke
BCMaterials
Basque Center for Materials
UPV/EHU Science Park, Leioa 48940, Spain

response,[5] and the embedding of magnetic NPs in the interior of RBCs to enable magnetic alignment and guidance.[6] So far, four main strategies have been developed for RBC engineering: 1) Surface grafting—that modifies the RBC membrane by coupling of drugs/targeting agents;[7] 2) hypotonic loading—that employs the formation of transient pores in the plasma membrane in hypotonic solutions to allow the subsequent loading of drugs or NPs in the RBC inner volume;[2a,b] 3) surface hitchhiking—where functional NPs are noncovalently attached to the membrane;[4] and 4) cell-in-shell—wherein RBCs are encapsulated within a nanometric artificial shell made of, for example, polyelectrolytes, polydopamine, or iron-phenolic networks.[5,8] Despite the success achieved to date for RBC functionalization, the current RBC engineering strategies still possess in general several limitations due to the RBC's fragile structure and susceptibility to extracellular environmental stress. First, most engineering approaches are time-consuming (e.g., hypotonic loading and layer-by-layer deposition of polyelectrolyte coatings) and conducted in specific, restrictive conditions.[5a] Second, the complex synthetic conditions of precursor chemistry/concentration, pH, temperature, and ionic strength often result in RBC lysis, excluding many classes of materials and strategies from being candidates for RBC functionalization.[5] Third, functionalized RBCs (e.g., created by surface modification with toxic chemicals or hypotonic loading of drugs/NPs) are often more fragile and environmentally sensitive than the parent RBC, or the RBC assemblies are not stable. These drawbacks limit their further bioapplications to a certain extent.[2a,b] Finally, most engineering procedures do not provide a versatile means to endow RBCs with combined/integrated multi-functionalities. These limitations urgently necessitate the development of a new RBC engineering/functionalization strategy.

Metal-organic frameworks (MOFs) are highly porous crystalline materials assembled through coordination between metal ions/metal nodes and organic linkers, showing both long-range and local structural order.[9] Due to their chemical diversity, tunable porosity, and high surface areas, MOFs have attracted tremendous interest for a wide range of applications such as gas storage and separation,[10] water harvesting,[11] sensing,[12] energy,[13] drug delivery,[14] and serving as nano-building blocks for the construction of complex hierarchical nanoarchitectures.[15] Inspired by the well-defined and modular chemistry of MOFs, here, we introduce the concept of "Armored Red Blood Cells" (armored RBCs). These are RBCs encapsulated within and surface engineered with functional, modular, MOF nano-building block-based exoskeletons (**Figure 1**). Exoskeletons are constructed within seconds through fast MOF NP super-assembly based on strong-multivalent metal-phenolic coordination[15b,c] and RBC/MOF complexation via multiple hydrogen-bonding interactions at the cellular interface (Figure 1a). The developed universal coating approach is highly biocompatible and easy to use. It does not introduce RBC hemolysis nor affect the normal physiology of RBCs in terms of oxygen-carrying capability, for example. It does not alter circulation behavior, as confirmed by the presence of reversible oxygenated and deoxygenated states, and long circulation times, as determined in chicken embryo and mice models. Depending on the type of MOF NPs or NP combinations, the physicochemical properties (like optical, magnetic, and sensing properties) of armored RBCs are highly tunable. The potential chemical diversity of armored RBCs is enormous, and here, various, functional MOF NPs including ZIF-8 (ZIF: Zeolitic imidazolate framework), MIL-100 (Fe) (MIL: Materials of Institut Lavoisier), UiO-66-NH_2 (UiO: Universitetet i Oslo), magnetic iron oxide (Fe_3O_4) NPs@ZIF-8, and hybrid mesoporous silica NP@MOF (MSNs, dye-labeled MSNs, sensing probe-loaded MSNs@ZIF-8), have been prepared as diverse armored RBC prototypes. The created armored RBCs not only show enhanced tolerance against external stressors such as antibody-mediated agglutination, detergents and pore-forming toxins capable of causing lysis, osmotic stress, and freezing, but they also possess abiotic properties including controlled disassembly, multifluorescence, magnetism, and blood nitric oxide (NO) sensing, which are utterly foreign to the native RBCs. In conclusion, the versatile RBC coating strategy holds great promise to promote the design of MOF/RBC-inspired functional microarchitectures for a wide range of bioapplications.

2. Results and Discussion

The presented approach of armored RBCs has a remarkable advantage for the design of multifunctional, hierarchical nanoassemblies: It can revert to the full range of MOF NPs as functional, robust, and modular building blocks. When constructing a multifunctional, protective shell around single RBCs, these MOF-based NPs rapidly form an exoskeleton based on particle-particle super-assembly and interlocking at the proximal RBC membrane surface. The exoskeleton assembly occurs in two steps: At first, MOF NPs concentrate near the membrane and attach to the native RBC surface. Since RBC membranes are rich in carbohydrates and proteins, they have a highly negatively charged surface.[16] Due to the frangibility and sensitivity of RBCs, strong, attractive interactions between NPs and RBC membranes always causes RBC hemolysis/rupture. MOF NP surfaces comprise well-defined, long, periodic arrangements of metal nodes and organic ligands, which allow precise tuning of the coordination and interactions with organic moieties on the RBC membrane surface. Based on zeta potential (ζ) measurements, MOF NPs used within this study (UiO-66-NH_2, MIL-100(Fe), and ZIF-8) have a negative charge ranging from −3.0 to −29.1 mV (Figure S1, Supporting Information, pH 7.4), which helps to avoid strong electrostatic interactions between the MOF NPs and the negatively charged RBC surfaces (ζ = −30 mV) and thereby prevents hemolysis; however, the electrostatic repulsion may limit MOF accumulation and attachment. To balance both contributions, we carefully chose an isotonic buffer (phosphate-buffered saline (PBS) at pH 5.0), in which the zeta potential of MOF NPs is strongly decreased from −29.1 to −11.5 mV for ZIF-8 MOF NPs. No hemolysis of RBCs occurs. Under these conditions, hydrogen bonding interactions between the organic ligands from MOF NPs and carbohydrates and proteins from RBCs drive MOF accumulation and attachment. The second step of exoskeleton assembly of armored RBCs involves interlocking of MOF NPs, that are already attached to the RBCs surface and additional exogenous MOFs via an interparticle ligand. We employed tannic acid as the interparticle ligand and added it sequentially to the MOF

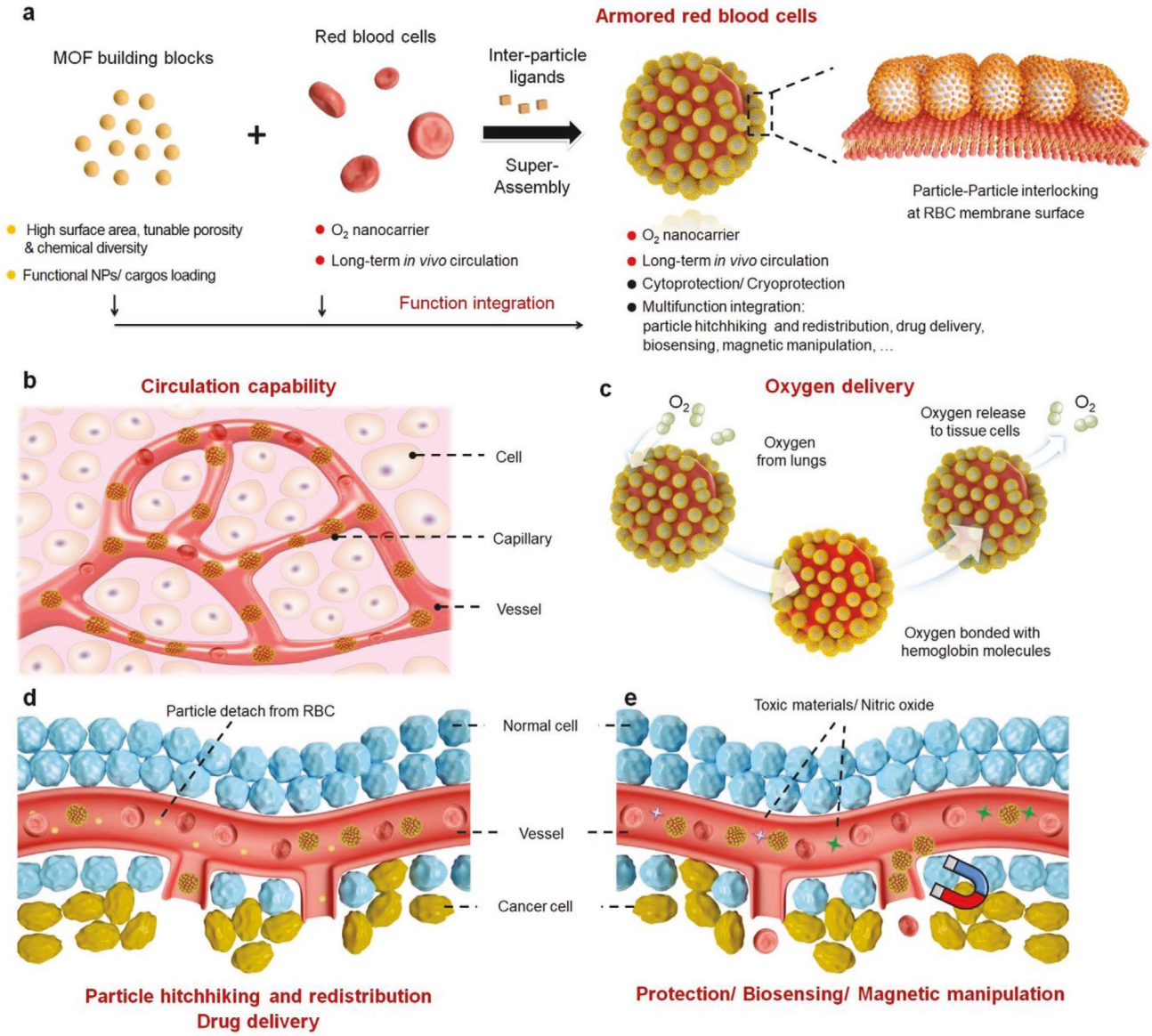

Figure 1. a) Schematic representation of armored RBC formation via immediate, multidentate ligand (tannic acid) assisted super-assembly of MOF nano-building blocks on the RBC membrane surface. Schematic illustration of the properties of armored RBCs: b) In vivo circulation, c) oxygen delivery, d) particle hitchhiking and redistribution, and e) enhanced resistance against external stressors and blood NO sensing.

NP/RBC mixed solution after a short incubation time (≈30 s). Tannic acid is frequently used as an organic building block[17] in MOFs, due to its well-known biodegradability and strong-multivalent coordination to various metal ions. Coupled with the additional strong metal-phenolic interactions, the colloidal MOF NP-based exoskeleton in armored RBCs can be created rapidly, in seconds. Using metal-phenolic chemistry, note that we successfully encapsulated mammalian cells with nanoparticle in an instantaneous process by suppressing the NP internalization pathways such as phagocytosis.[15c] In that case, NPs are very easy to be accumulated onto the mammalian cell membrane surface under normal physiological conditions, which is followed by cross-linkage. However, in this case, due to the varying surface chemistry between RBCs and mammalian cells and the strong impulse of RBC to lyse, the formation mechanism is quite different. Only when the balance of interactions (electrostatic repulsion/hydrogen bonding caused attraction) between RBC and NPs is achieved, NPs assemble around the RBC surface (Figure S2, Supporting Information).

As a demonstration of the armored RBC concept, individual, purified RBCs (**Figure 2**a) encapsulated within UiO-66-NH_2 MOF NP-based exoskeletons (termed armored RBC-UiO-66-NH_2) were constructed via the sequential addition of a colloidal UiO-66-NH_2 NP solution and tannic acid to RBC suspensions (see Materials and Methods in Supporting Information for detailed information). We synthesized colloidal UiO-66-NH_2 MOF NPs with a diameter of ≈440 nm according to reported solvothermal methods.[18] Transmission and scanning

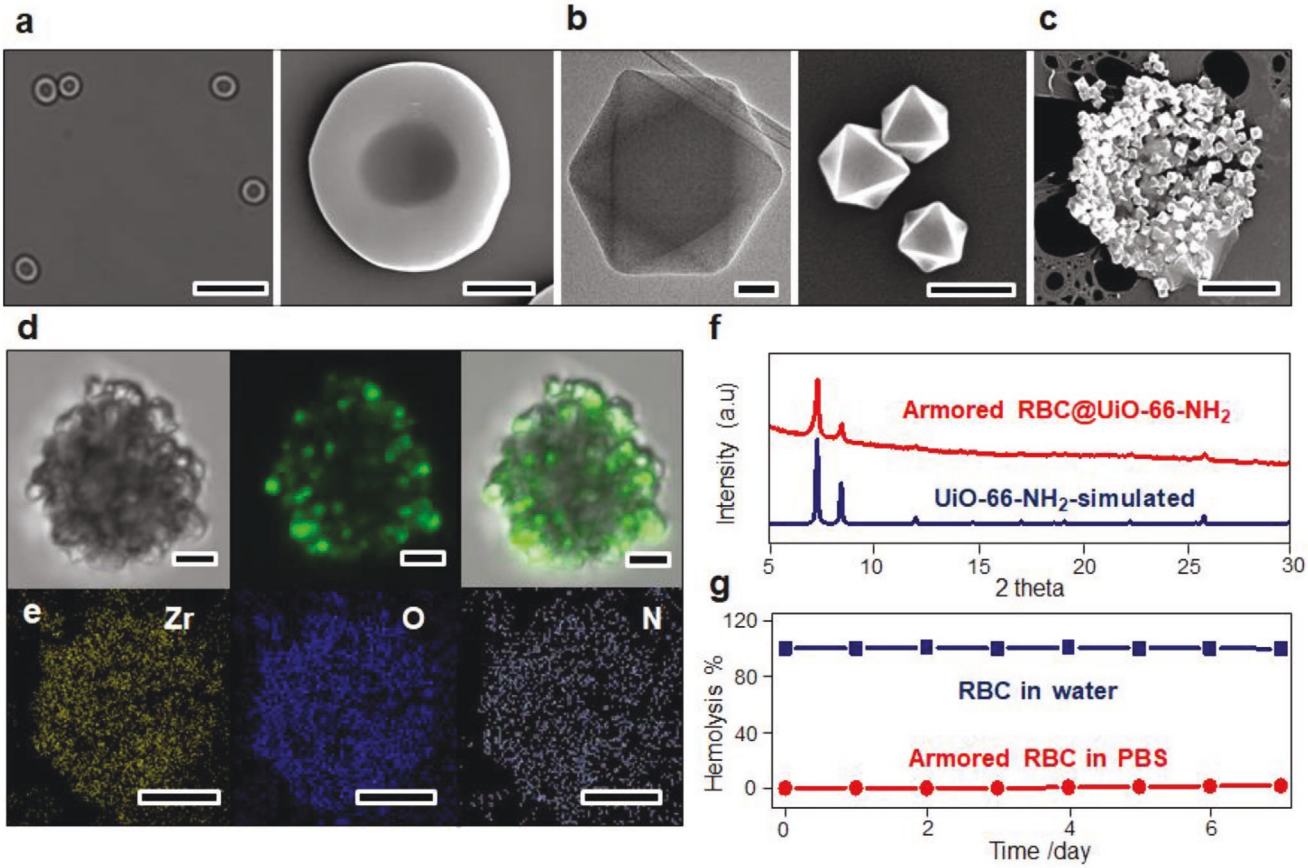

Figure 2. a) Bright-field (left) and SEM (right) image of RBCs. Scale bars, 25 µm (left), 2 µm (right). b) TEM and SEM image of UiO-66-NH_2 MOF NPs. Scale bars, 50 nm (left), 500 nm (right). c) SEM image of the armored RBCs-UiO-66-NH_2. Scale bar, 5 µm. d) DIC, confocal fluorescent, and combined image of armored RBCs-UiO-66-NH_2 labeled with fluorescein isothiocyanate (from left to right). Scale bars, 5 µm. e) SEM mapping (Zr, O, and N) of armored RBCs-UiO-66-NH_2. Scale bars, 5 µm. f) Wide XRD patterns of the synthesized armored RBCs-UiO-66-NH_2 and the simulated UiO-66-NH_2 crystals. g) Time-dependent hemolysis of armored RBCs@UiO-66- NH_2 in 1x PBS solution and RBCs in water as a control.

electron microscopy (TEM, SEM) (Figure 2b) and wide-angle X-ray diffraction (XRD) (Figure 2f) confirmed their crystalline structures with well-defined octahedral shapes. The formation of UiO-66-NH_2-based exoskeletons surrounding RBCs is clearly visible in the SEM image, as shown in Figure 2c. The roughened surface (Figure 2c), which is due to a dense packing of NPs at the RBC surface, is further visible in bright field images (Figure S3, Supporting Information). Fourier-transform infrared spectroscopy performed on armored RBC-UiO-66-NH_2 (Figure S4, Supporting Information) confirmed the presence of UiO-66-NH_2 MOF NPs, as determined by the characteristic peaks at 1570 and 1256 cm^{-1} assigned to the $-CO_2$ asymmetrical stretching and C—N vibrational bands, respectively, of the aminocarboxylate groups of UiO-66-NH_2. Analyzing nearly 50 armored RBCs by bright-field optical microscopy and SEM imaging supported the fact that all erythrocytes were encapsulated within homogeneous conformal exoskeletons. This could be further confirmed by confocal laser-scanning microscopy of fluorescein isothiocyanate-labeled UiO-66-NH_2 NP-based exoskeletons. A uniform and homogeneous UiO-66-NH_2-NP layer that encapsulates the RBC can be observed (Figure 2d). Moreover, energy-dispersive X-ray spectroscopy for mapping of zirconium, oxygen, and nitrogen atoms (Figure 2e) along with wide-angle XRD (Figure 2f) further confirmed, that the structural and chemical integrity of UiO-66-NH_2-NPs is preserved within the exoskeleton. Importantly, the structure of the armored RBC-UiO-66-NH_2 is still stable after long-term storage. The fast coating process did not cause the hemolysis of RBCs even after 7 days of storage (Figure 2g), indicating that the formed exoskeleton has no toxic effects on RBCs.

To demonstrate the generality of the armored RBC approach, that is, the protective and functional encapsulation of native RBCs by diverse types of MOF NPs via spontaneous superassembly, we tested MIL-100(Fe), magnetic Fe_3O_4 NPs@ZIF-8, and hybrid MSNs@ZIF-8 in different shapes, sizes, and functionalities as building blocks for the design of various armored RBCs. For every case, successful preparation of NP was confirmed by a panel of analyses including XRD, SEM, TEM, and dynamic light scattering (Figures S5–S9, Supporting Information). Note that the used MOF NPs, such as UiO-66-NH_2 and MIL-100 (Fe) NPs are stable in PBS or weak acidic solution.[14a] For ZIF-8 MOF NPs, it has been reported that ZIF-8 MOF NPs are acid-responsive NPs and stable in PBS but can be degraded in acid solution after a couple of hours.[14a,c] Nevertheless, in our

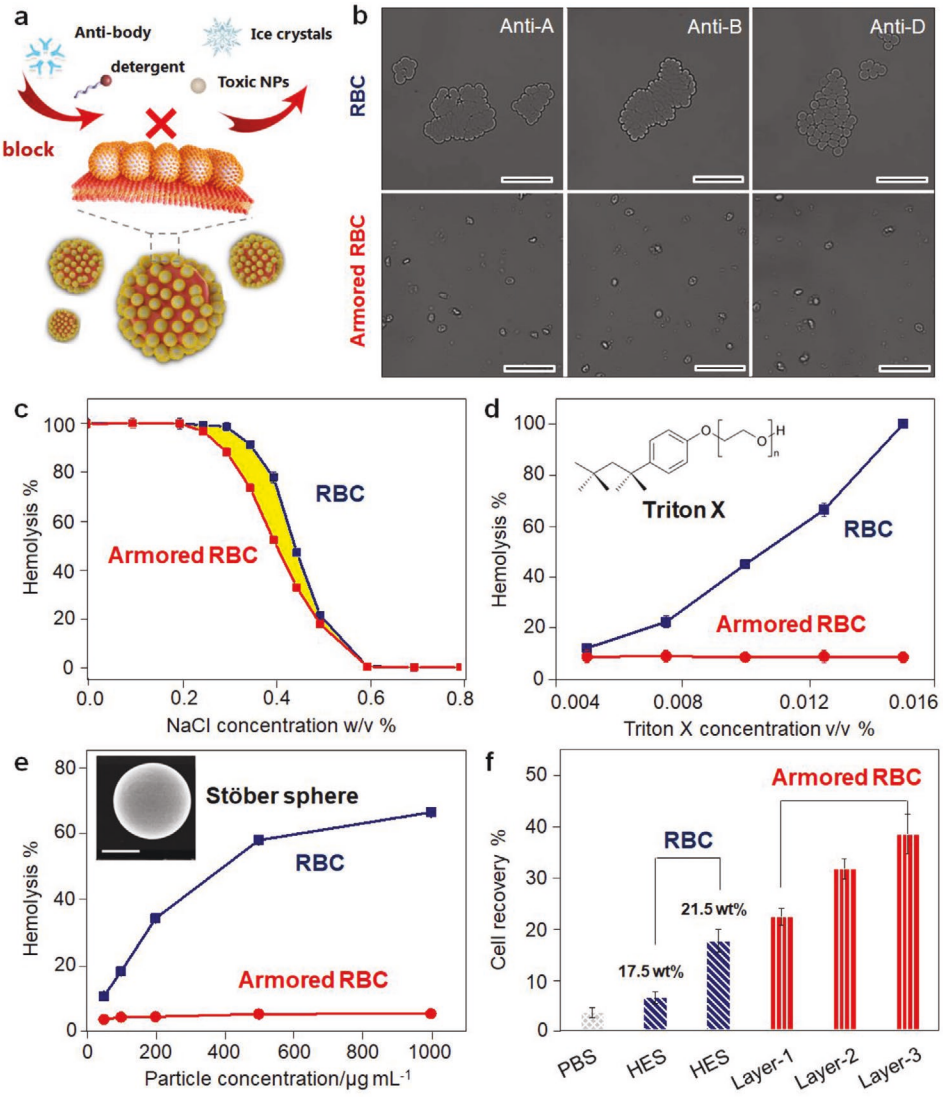

Figure 3. a) Schematic illustration of the protection of RBCs against external stressors based on MOF NP encapsulation. b) The optical images of human type A, B, and Rh RBCs in their corresponding anti-typing sera. Scale bar, 50 μm. Hemolytic behavior of native RBCs and armored RBCs-MIL-100(Fe) as a function of c) NaCl concentration (i.e., osmotic pressure stimulus), d) Triton X-100 concentration (i.e., detergent stimulus), and e) Stöber particle concentration (i.e., NP stimulus). Scale bar is 300 nm. f) The recovery of native RBCs cryopreserved in HES polymer (175 or 215 mg mL^{-1}) PBS dispersions, and armored RBCs cryopreserved in PBS solution and protected by MIL-100(Fe) NP-based exoskeletons with increasing coating cycles.

case, although the construction condition for armored RBCs was in pH 5.0 solution, the super-assembly process was finished in only 1 min and then the buffer was exchanged to 1x PBS solution (pH 7.4). The short exposure time did not affect the structure of ZIF-8. The stability of the used MOF NPs in PBS is the prerequisite for the construction of armored RBCs. The full characterization and description of each of these armored RBC types appear below. The results clearly demonstrate that the armored RBC approach is a powerful and universal strategy to create multifunctional, cellular super-assemblies since it is fast and easy.

The first impressive property of armored RBCs is their enhanced cytoprotection against external stressors. To benchmark the protective effect, we exposed armored RBC-MIL-100(Fe) to various harsh environmental conditions including antibody-mediated agglutination, osmotic pressure, detergents, toxic NPs, and freezing conditions (**Figure 3**a). The bright-field image in Figure S10, Supporting Information, confirmed the successful assembly of MIL-100(Fe)-NP-based exoskeleton. At first, antibody-mediated agglutination assays were performed (Figure 3b) to assess the blood group antigen immunogenicity of armored RBCs.[5a] As shown in Figure 3b (top row), native RBCs of type B rapidly and severely agglutinated in presence of small amounts of anti-B serum. Identical results were obtained with type A and type RhD-RBCs in their corresponding anti-type anti-sera; on the contrary, no antibody-mediated aggregation was observed in armored RBCs, even with the extension of exposure time (Figure 3b—bottom row). Armored RBCs possess a highly effective immune-protective exoskeleton that shields the immune-response provoking epitopes on RBC surfaces against agglutination. Second, the tolerance of armored

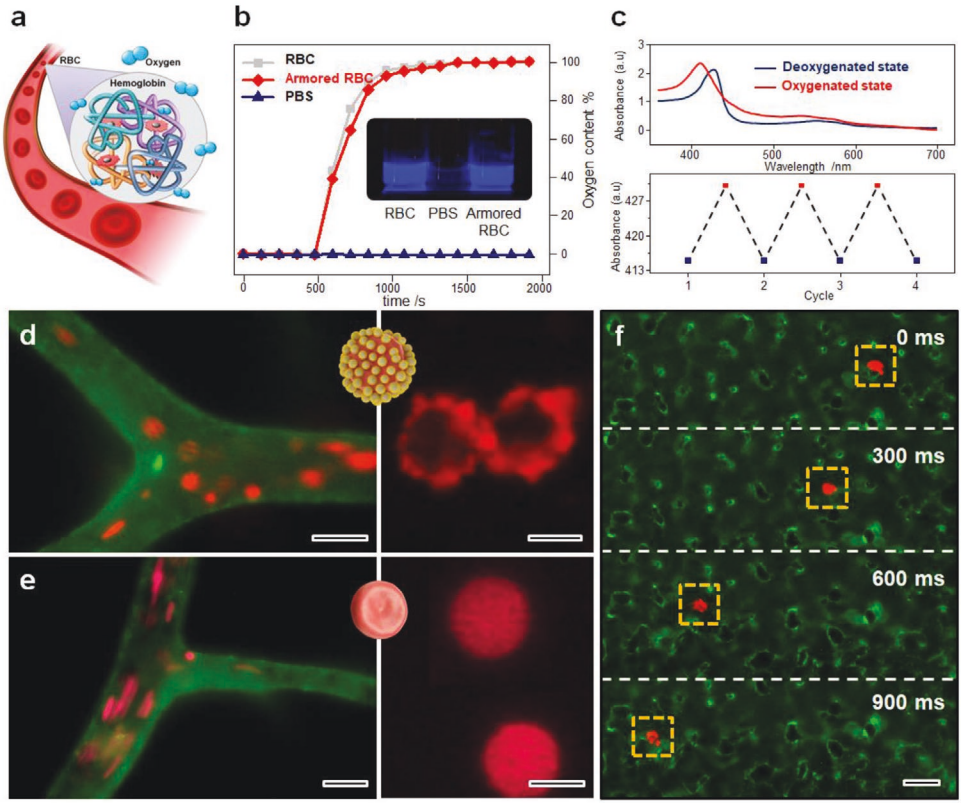

Figure 4. a) Schematic illustration of oxygen binding via hemoglobin by RBCs. b) Time-dependent oxygenation curves of native RBCs and armored RBC-MSN@ZIF-8. Insert images show the generation of the bluish glow of native and armored RBCs after the addition of the luminol-perborate mixture. c) UV–vis spectra of the oxygenated and deoxygenated states of armored RBC-MSN@ZIF-8 (top) and the related reversible transfer between two states (bottom). The circulation of d) armored RBC-MSN@ZIF-8 and e) native RBCs in the vessel of a chick embryo in the chorioallantoic membrane (CAM model (left)), and the related (confocal) fluorescence images (right). Scale bars are 50 μm (left), 5 μm (right). f) The flow of armored RBC-MSN@ZIF-8 within the CAM capillary bed. Scale bar is 20 μm.

RBCs to osmotic pressure was tested, and the percentage of cells undergoing hemolysis was measured. At first glance, the osmotic fragility curves of both native RBCs and armored RBCs showed similar rupture profiles (Figure 3c). Cellular fractures of native and armored RBCs were initiated at a concentration of NaCl of 0.60% (w/v), but native RBCs burst fully at a concentration of 0.30%, while the burst concentration of armored RBCs was shifted to 0.20%. The enhanced tolerance to osmotic pressure can be attributed to two sources/contributions. On the one hand, the enhanced membrane reinforcement provided by the MOF exoskeleton offers a physical restriction that delays the swelling process. On the other hand, the potential adsorption of ions in MOF pores may delay the ion transfer from the external medium to RBC intracellular fluids.[19] Both effects could lead to a reduced and delayed RBC lysis under hypotonic conditions. Next, the hemolytic protection of armored RBCs exposed to the nonionic detergent Triton X-100 and so-called "Stöber" amorphous silica NPs was tested, since both species are known to easily cause RBC lysis. As shown in Figure 3d,e, a slight change in Triton X-100 concentration or particle concentration greater than 500 μg mL^{-1} already led to massive lysis of RBCs, whereas armored RBCs exhibited negligible hemolysis under both conditions. We attribute this cytotoxic agent resistance to a physical barrier effect provided by the armored shell. Finally, we determined the resistance of armored RBCs to freezing conditions in comparison to native RBCs. Ice recrystallization is the major challenge during cryopreservation of RBCs.[20] The formation of ice crystals not only imparts serious mechanical damage to the delicate RBCs but also creates increased osmotic pressure across the cell membrane, leading to the rupture of RBCs. In order to provide extensive ice recrystallization and maximize cell stress during the cryopreservation test, both native RBC and armored RBC samples were rapidly frozen in liquid nitrogen (–196 °C) for 2 h and then slowly thawed at 4 °C over several hours. As shown in Figure 3f, the native RBC recovery in PBS buffer is very low (<5%). However, protected by the armored shell, the cell recovery increased to ≈25%. With further increase of coating cycles to get a thicker shell, the cell recovery of RBCs can be increased up to 40% without the addition of any toxic solvents. This cell recovery is superior to that obtained via commonly used hydroxyethyl starch polymers at a concentration of 17.5 and 21.5 wt%, highlighting the excellent protection conferred by the MOF NP-based exoskeletons.

A crucial feature of RBCs is their oxygen carrier capability and long-circulation times in blood. To check the related behaviors of our designed armored RBCs, at first, we employed luminol-based chemiluminescence to reveal the presence of hemoglobin in armored RBCs (**Figure 4**a). Note, that ZIF-8

NPs-based armored RBCs are used for later discussion in this part since ZIF-8 MOF NPs can be easier fluorescently labeled than MIL-100 (Fe) NPs. When hemoglobin and luminol-perborate come in contact upon mixing, the iron in the hemoglobin accelerates the reaction of luminol with the peroxide generated from perborate, which results in a bluish glow (Inset of Figure 4b). After the addition of luminol-perborate in solution, both native RBCs and armored RBCs-MSN@ZIF-8 become chemiluminescent after 10 min. This finding clearly shows that the armored shell does not inhibit the iron catalytic properties of intracellular hemoglobin within RBCs. The inherent porosity of the armored shell—attributed from the pores inside MOF NPs and the voids between MOF NPs—provides full accessibility of small molecules such as luminol and peroxide to the RBC and permits access to and crossing of the RBC membrane. To investigate the oxygen carrier capability, UV–vis spectroscopy was used to reveal the reversible shift of maximum absorption peaks of RBCs in oxygenated and deoxygenated states (Figure 4c and Figure S11, Supporting Information). The characteristic absorption peak of native RBCs and armored RBCs in an oxygenated state appeared at 415 nm (Figure 4c). After bubbling nitrogen for 2 h and adding the reducing agent sodium dithionite ($Na_2S_2O_4$), the absorption peak red-shifts to 430 nm, confirming the switch to the deoxygenated state for both native RBCs and armored RBCs. The deoxygenated state can carry oxygen again after exposure to atmospheric oxygen. The process of binding and releasing oxygen was repeatable (Figure 4c), demonstrating that the capability of armored RBCs to carry oxygen was preserved. By comparing the oxygenation rate of both deoxygenated samples, as shown in Figure 4b, the time-dependent oxygenation curves of native and armored RBCs showed similar behaviors, while a delay of about 60 s was found for armored RBCs. We explain this observation by the presence of the porous MOF shell that increases the tortuosity of the oxygen diffusion pathway, and thus causes oxygen molecules to spend more time trapped within MOF pores.

RBCs are well known to easily traverse the microvasculature with dimensions that are smaller than their size and display long circulation times in vivo. To investigate the circulation behavior of armored RBCs, we carried out real-time fluorescence wide-field imaging on a chick embryo ex ovo (chorioallantoic CAM model; Figure S12, Supporting Information), that provides easy and direct optical access for intravital imaging of the flow of RBCs in blood vessels. Alexa Fluor 647-labeled MSN@ZIF-8 hybrid NPs with a diameter of ≈80 nm were used as building blocks for armored RBC construction (Figure S13, Supporting Information). A coherent, conformal NP layer encapsulating RBCs, clearly observed in Figure 4d, confirmed the successful formation of armored RBCs. The blood vessels are labeled with fluorescein-labeled lens culinaris agglutinin for direct visualization. The flow of the armored RBCs was not affected, even after circulating for 30 min, as shown in Figure 4d,f and Video S1, Supporting Information, compared to the flow of the DiD-labeled native RBCs in the blood vessels and capillaries (Figure 4e, Figure S14 and Video S2, Supporting Information). The flow supports normal circulation properties, despite the armored RBCs shape exhibiting a certain degree of deformation compared to native RBCs.

Before further characterizing the circulation properties of the armored RBCs in vivo, we assessed the cytotoxicity of armored RBCs as well as their in vivo toxicity. For this, different types of MOF NPs (UiO-66-NH_2, MIL-100, ZIF-8, MSN@ZIF-8, and Fe_3O_4@ZIF-8) were used to generate armored RBCs and investigate the biocompatibility. As shown in Figure S15, Supporting Information, none of the armored RBCs with MOF NPs exhibited significant hemolysis activity even after storage for 5 days, indicating the non-toxicity of formed NP exoskeleton on armored RBCs. In addition, the cytotoxicity of MOF NPs themselves and armored RBCs with MOF NP to HeLa and A549 cells were examined. There was no cytotoxicity of MOF NPs and armored RBCs up to a concentration of 200 μg mL^{-1} NPs themselves (Figure S16, Supporting Information) or NPs on armored RBCs (Figure S17, Supporting Information). To further analyze their biocompatibility, a in vivo toxicity study has also been processed based on body weight, blood biochemistry, and tissue histopathology. Albino C57BL/6 mice were intravenously administered with PBS (control), MSN@ZIF-8 NPs (1 mg NP per mice), or armored RBCs-MSN@ZIF-8 (armored RBCs with 1mg NP per mice). After 4 weeks, the mice were euthanized, the blood was collected for analyzing blood cell population and blood metabolites, and the major organs were excised, sectioned, and examined for morphological changes. During the treatment period, there is no clear weight difference between the armored RBCs treated group and the healthy control (PBS) group, as well as the group treated only with MSN@ZIF-8 NPs (**Figure 5**a). Additionally, all three groups displayed similar parameters of blood cell population and blood metabolites after treatment (Figure 5b–f). It is noted that there were no statistically significant differences between three groups for alkaline phosphatase, alanine aminotransferase (ALT) and blood urea nitrogen (Figure 5d), indicating that even at this high dose (1 mg per mice, about 50 mg kg^{-1}) armored RBCs did not impact the normal function of the liver or kidney. Furthermore, hematoxylin and eosin (H&E) staining of the liver, lung, kidney, spleen, and heart sections did not show any signs of abnormality in cellar morphology, inflammation, or tissue organization in the treated group compared with the control group (Figure 5g), further indicating that armored RBCs have little or no side effects on mice. These findings confirm the overall biocompatibility of armored RBCs.

To examine the pharmacokinetics and biodistribution behaviors of armored RBCs, albino C57BL/6 mice were injected with control DyLight 800-labeled MSN@ZIF-8 hybrid NPs and the corresponding MSN@ZIF-8 armored RBCs by retro-orbital injection[21] at a dose of 150 μg NPs per mouse. Syngeneic RBCs were used to create armored RBCs, negating blood cell type complications. To study the circulation half-life at various time points following the injection (**Figure 6**a), blood was collected from the eye socket of the mice to evaluate the concentrations of circulating control NPs or armored RBCs. At 12 h and 24 h post-injection, the armored RBCs exhibited 19% and 15% overall retention in mice blood, respectively, as compared to the 6% and 2% shown by control NPs (Figure 6d). The semilog plot of retention-circulation time (Figure S18, Supporting Information) illustrates a bi-exponential decrease in particle concentration over time, indicating that both NP and armored RBC circulation follow a two-compartment pharmacokinetic model.[4,22] After

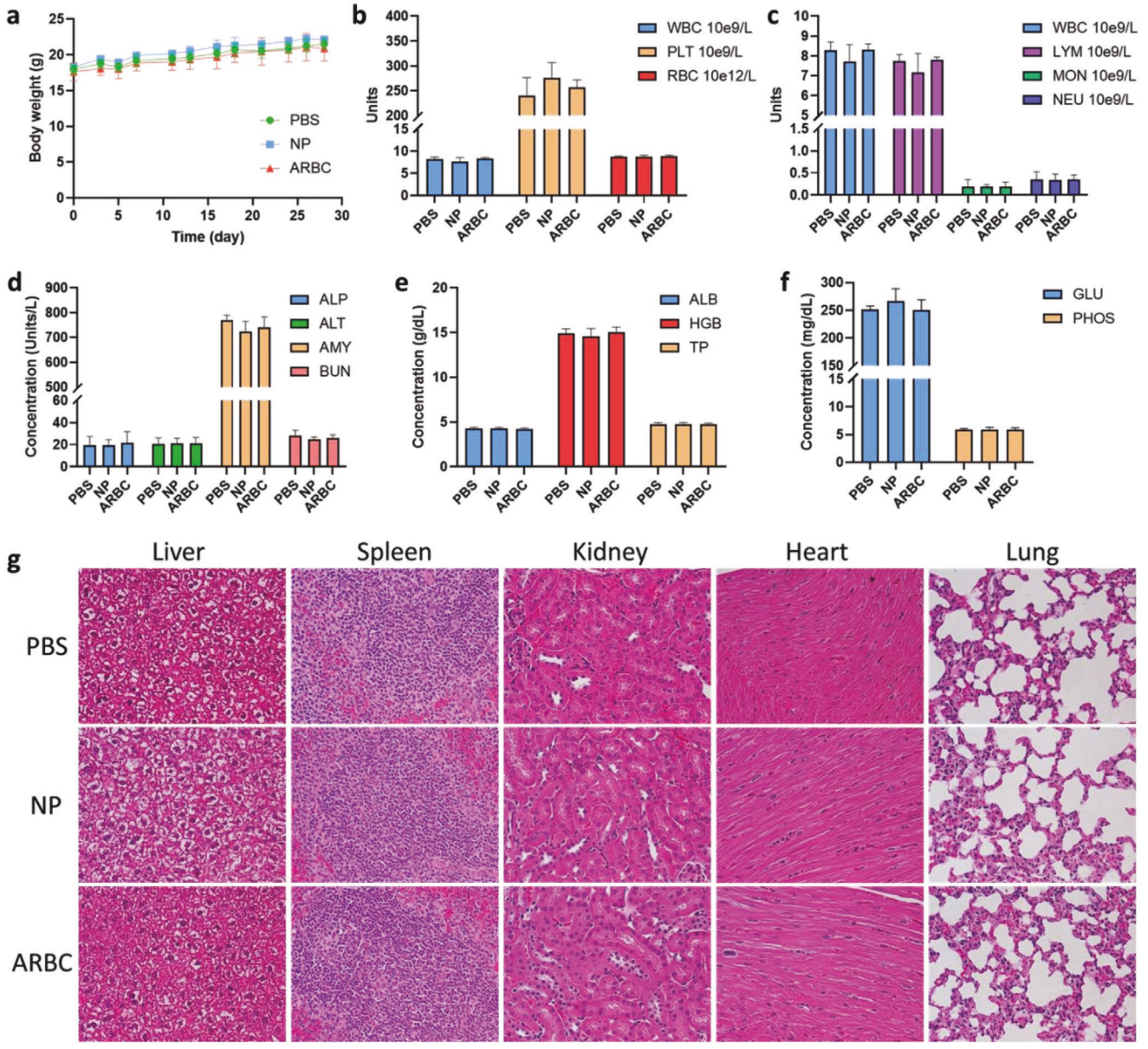

Figure 5. a) Body weight of mice during the in vivo toxicity study. (mean ± SD, $n = 4$, two-tailed t-test, not significant). b) White blood cell (WBC), platelet (PLT), and red blood cell (RBC) cell counts (mean ± SD, $n = 4$, two-tailed t-test, not significant). c) White blood cell (WBC), lymphocyte (LYM), monocyte (MON), and neutrophil (NEU) cell counts (mean ± SD, $n = 4$, two-tailed t-test, not significant). d) Alkaline phosphatase (ALP), alanine aminotransferase (ALT), amylase (AMY), and urea nitrogen (BUN) level (mean ± SD, $n = 4$, two-tailed t-test, not significant). e) Albumin (ALB), hemoglobin (HGB), and total protein (TP) level (mean ± SD, $n = 4$, two-tailed t-test, not significant). f) Glucose (GLU) and phosphorus (PHOS) level (mean ± SD, $n = 4$, two-tailed t-test, not significant). g) Histological analysis of explanted organs liver, spleen, kidney, heart, and lung using hematoxylin and eosin staining of the control group, NP-treated group and armored RBC-treated group indicated no signs of cellular or tissue damage.

fitting to the two-compartment pharmacokinetic model, numerical analysis (Figure 6d) indicated that the elimination half-life of NPs and armored RBCs was 16.0 ± 3.7 and 66.3 ± 17.4 h, respectively. Armored RBCs displayed a remarkably enhanced retention in blood circulation in comparison with control NPs. Our finding is well correlated with reports that anchoring nanoparticles onto the RBC surface could prolong the intravascular particle circulation, where the flexibility, circulation, and vascular mobility of RBCs could help the adhered nanoparticles to escape rapid reticuloendothelial system (RES) clearance.[4]

Furthermore, to analyze the related biodistribution, at 12 and 24 h post-injection, mice were euthanized and their liver, spleen, kidneys, heart, lungs, and blood were harvested for fluorescence analysis (Figure 6b). The majority of fluorescence signal was found in the two primary filtering organs, the liver and spleen after 12 h post-injection, supporting removal by the RES. However, the fluorescence intensity from the armored RBCs in the spleen decreased 24 h post-injection and simultaneously increased in the lungs, suggesting detachment of MOFs from the RBC surface and their return into circulation

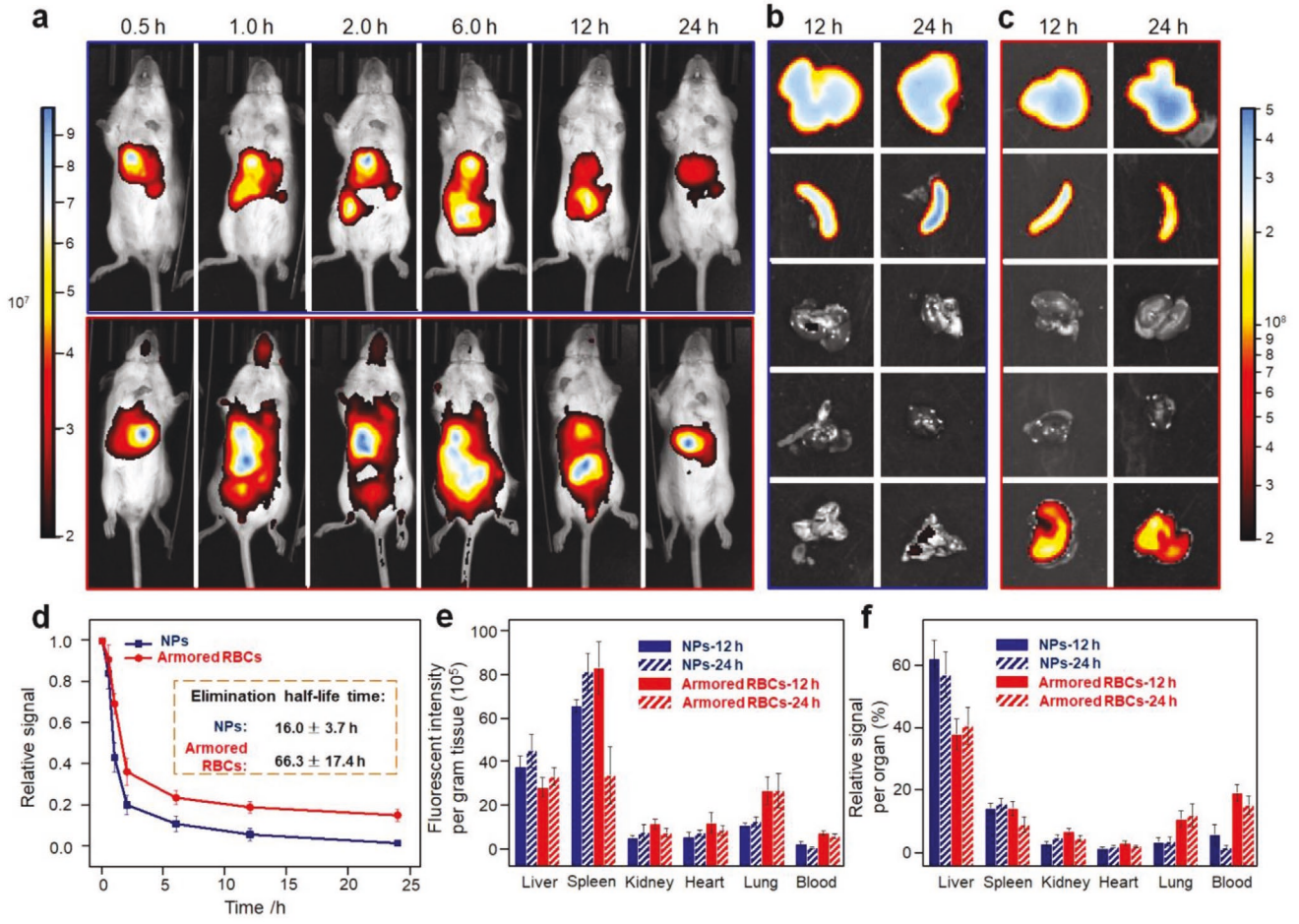

Figure 6. a) Whole mice fluorescence images acquired using the IVIS Spectrum at 0.5, 1, 2, 6, 12, and 24 h after intravenous administration of DyLight 800-labeled MSN@ZIF-8 hybrid NPs (top) and the related armored RBCs (bottom), respectively. Fluorescence images of different organs (liver, spleen, kidney, heart, and lung from top to bottom) at 12 and 24 h after intravenous administration of b) NPs and c) armored RBCs, respectively. d) Circulation time of both NPs and armored RBCs ($n = 3$; mean ± SD). Insert table is the related elimination half-life. e) Fluorescence intensity per gram of tissue and f) relative fluorescence signal per organ at 12 and 24 h after intravenous administration of NPs and armored RBCs ($n = 3$; mean ± SD).

(Figure 6a). Notably, 24 h after injection, the optically labeled armored RBCs exhibited a tenfold higher blood persistence and 3.5-fold higher accumulation in the lungs compared to the control NPs (Figure 6e,f). It was postulated that NPs from armored RBCs accumulate in the lungs following release caused by squeezing through tiny capillaries in the lung vasculature.[4,22] The high cardiac blood output can cause shear forces that could facilitate the transfer of the NPs from the RBC surface to pulmonary capillary endothelial cells. Note that the in vivo stability or in vivo detachment behavior of armored RBCs are very hard to be characterized at this moment, and will be investigated in the future with the collaboration of other experienced research groups. In summary, our created, armored RBCs exhibit enhanced in vivo circulation/residence times compared to many other classes of nanoparticles[4] and could serve as sources of MOFs (or conceivably other NPs) that could be released and targeted to various organs over time. This could extend the in vivo applications of MOFs.

Given the chemical diversities of MOF nano-building blocks, the armored RBC concept can be generally extended with a plethora of MOF types and combinations. It is basically unlimited in generating diverse functionalities and hence serves as a promising technology to satisfy the growing need of multifunctional NPs in biomedical applications, which we demonstrate in the following section. Depending on the MOF building block, armored MOF shells can i) not only be assembled but also biocompatibly disassembled if necessary. Depending on the underlying MOF NPs, armored RBCs offer ii) unique physiochemical properties such as optical, magnetic, and sensing properties. But most importantly: iii) The armored RBC concept profits enormously from multiplexing: MOF NP associated properties can be linearly combined within the armored RBC shell during a mixed super-assembly synthesis.

First, as an "armed armor" of armored RBCs, the detachability of the armored shell is an important feature of this construct. Due to the responsive nature of the metal-phenolic complexation, the armored MOF shell can be disassembled in ethylenediaminetetraacetic acid (EDTA) solution in a programmed fashion. As shown in **Figure 7**a, the armored MOF shell can be progressively disassembled over the time course of 15 min (as shown by fluorescence microscopy for UiO-66-NH_2-covered RBCs labeled with fluorescein isothiocyanate. Note that the EDTA etching solution (20 mM, pH 7.4) has a negligible impact on RBCs. Upon EDTA-induced detachment

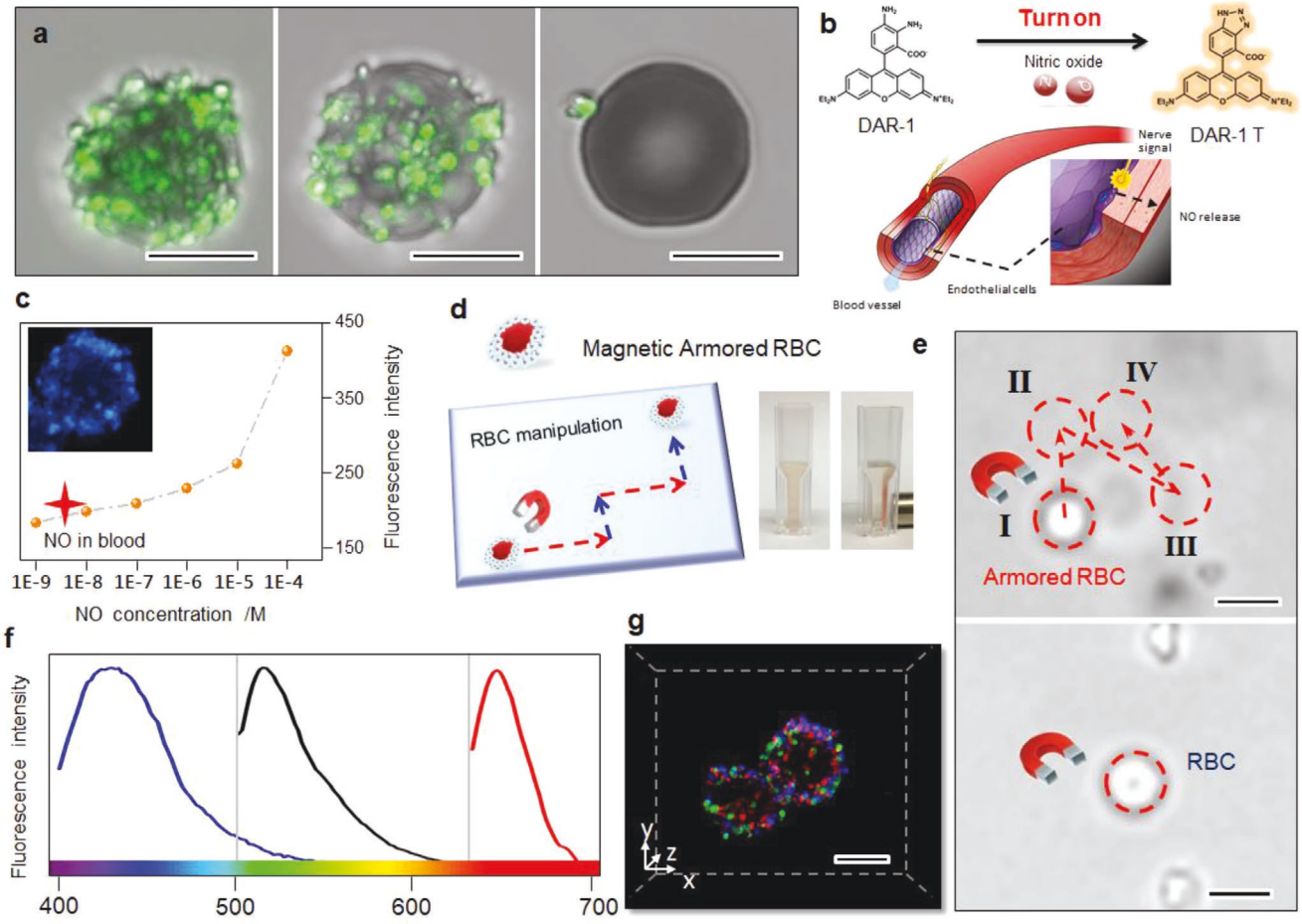

Figure 7. a) Controlled disassembly of the shell leads to a reversible recovery of the RBC normal state for armored RBC-UiO-66-NH_2 labeled via fluorescein isothiocyanate. The etching time in presence of EDTA amounted to 0, 5, and 15 min. Scale bars, 5 µm. Armored RBCs serving as a sensor. b) Schematic illustration of the sensing of NO within blood vessels based on the use of the fluorescent probe of DAR-1. c) Calibration curve: Fluorescent intensity change versus NO concentration. The red star points out the NO concentration in fresh blood based on the sensing function of DAR-1 loaded armored RBCs. Insert fluorescent image is DAR-1-loaded armored RBCs after incubation in NO solution (100 µM) for 5 min. d) Schematic illustration of the manipulation of magnetic armored RBCs via an external magnetic field (left). Photographs of a dispersion of magnetic armored RBCs before (left) and after (right) magnetic extraction from a vial. e) Bright-field microscopy images of magnetically-actuated armored RBC-Fe_3O_4@ZIF-8 (left) or immobile RBCs (right). Scale bars, 10 µm. f) Fluorescence spectra of multi-fluorescent armored RBCs-MSN@ZIF-8 with emission at 428, 515, and 648 nm. g) Multimodal armored RBCs. Confocal images of multi-fluorescent armored RBCs based on three different fluorescent MSN@ZIF-8 nano-building blocks. Scale bar, 5 µm.

of MOF NPs for 15 min, the armored MOF shells were almost completely removed and no defects were observed on the RBC surface, which suggests that the RBCs can reversibly return to their original morphology. This on-demand protective shell formation and degradation capability provide RBCs a capability reminiscent of the germination of natural spores.

Second, to demonstrate the sensor capabilities of armored RBCs, we employed the modular properties of MOF NPs to design armored RBCs that detect nitric oxide (NO) in blood. NO is a key signaling molecule acting as a potent vasodilator that relaxes the arteries (Figure 7b).[23] Hybrid MSN@ZIF-8 NPs (Figure S13, Supporting Information) were used as exoskeleton building blocks wherein 4,5-Diamino-rhodamine B (DAR-1), serving as a fluorescent probe, was pre-loaded within the MSN mesopores. NO-triggered fluorescence was observed for the DAR-1 probe, after its ring-closure and transition from the weakly fluorescent diamino structure to the strongly fluorescent triazole state.[24] The sensitivity of designed DAR-1-loaded armored RBCs was determined by exposing the encapsulated cells to freshly prepared NO solutions with different NO concentrations. The fluorescence intensity increases monotonically with increasing NO concentration (Figure 7c), which we determined as integrated fluorescence over the sample cuvette via fluorescence wide-field imaging of DAR-1-loaded armored RBCs (see, for example, Figure 7c (inset) at 100 µM NO and 5 min incubation time). By incubating our sensing armored RBCs in fresh blood for 5 min, the NO concentration in fresh blood could be determined to be 8.6 nM, which is in line with literature values.[25] This study demonstrates the potential of our designed armored RBCs as sensors not only for real-time monitoring and detection of NO in blood but also for further measurements like cellular pH or ROS and redox potentials depending on chosen fluorophores.[26]

Thirdly, armored RBCs inherit the collective properties of their MOF or other NP building blocks imparting desirable non-native properties. To demonstrate this idea, we created

magnetic armored RBCs that can be externally controlled. Based on metal-phenolic linker chemistry, magnetic Fe_3O_4 (≈8.0 nm) embedded in ZIF-8 MOFs (Figure S19, Supporting Information) were super-assembled onto the RBC surface to form a magnetic armored shell. In contrast to native RBCs, the magnetic armored RBCs can be manipulated now via an external magnetic field (Figure 7d,e). This property is of interest for 3D cell patterning and micro-motorized cellular constructs.[6a,b]

Finally, modular super-assembly of armored RBCs provides far-reaching possibilities for extensions via coassembly of different functional MOF- (or NP-) based nano-objects into multimodal nano-structures. To introduce armored RBCs as a multimodal super-architecture, we created multi-fluorescent RBCs by incubating native RBCs simultaneously with almost equal concentrations of three different fluorescently labeled MSN@ZIF-8 NPs in a one-pot process for less than 2 min (Figure 7f,g). The fluorescence spectra of the resulting armored RBCs featured three distinct emission peaks at 428, 515, and 648 nm (Figure 7f). Confocal fluorescence microscopy images in 3D demonstrated the formation of a continuous exoskeleton and a homogeneous distribution of NPs that preserved the stoichiometry of the synthesis solution (Figure 7g). This example suggests that the coassembled armored MOF shell could introduce a nearly infinite number of functionalities to armored RBCs and might provide efficient coupling effects between the functional MOF NPs.

3. Conclusion

We have developed a general, simple, and modular approach to creating a class of hybrid biomaterials termed armored RBCs with diverse possible functionalities. Using metal-phenolic chemistry, we encapsulated native RBCs with MOF NP-based exoskeletons in seconds without RBC lysis. The modularity and simplicity of this method arises from fast MOF NPs super-assembly at the RBC membrane surface and enables the transformation of different MOF building blocks and RBC vehicles into diverse functional hierarchitectures. The presented armored RBCs preserve the original properties of native RBCs, show enhanced resistance against external stressors, and exhibit extraordinary properties that are foreign to native RBCs based on the highly modular nature of MOF nano-building blocks integrated into the RBC exoskeletons. The presented approach profits from the wide range of variable MOF NPs and opens the door to the design of multimodal nano-superstructures for wide ranging bioapplications.

4. Experimental Section

Synthesis of Armored Red Blood Cell with Metal-Organic Framework Nanoparticles: RBCs were suspended in 1X PBS (pH 5) solution containing MOF NPs. After 10 s vortexing and 20–30 s of incubation, tannic acid in 1X PBS (pH 5) solution was added with 30 s vigorous mixing. The formed armored RBC was then rinsed with 1X PBS (pH 7.4), and stored in 1X PBS (pH 7.4). This process represents a typical procedure for single MOF NP shell formation and could be repeated one or two times to achieve multi-layered coating. Detail protocols for each different MOF NP are shown in Supporting Information.

Test of Vascular Flow in Ex Ovo Chick Embryos: The vascular flow characteristics of armored RBCs were tested using the ex ovo chick embryo model as described previously and was conducted following institutional approval (Protocol 11-100652-T-HSC). Briefly, eggs were acquired from East Mountain Hatchery (Edgewood, NM) and placed in a GQF 1500 Digital Professional incubator (Savannah, GA) for 3 days. Embryos were then removed from shells by cracking into 100 mL polystyrene weigh boats. Ex ovo chick embryos were covered and incubated at 37 °C, 100% humidity. 20 million cells mL^{-1} of DiD-labeled native RBCs and Alexa Fluor 647-labeled-armored RBC-MSN@ZIF-8 were incubated in 1X PBS (pH 7.4) solution with 10 mg mL^{-1} bovine serum albumin (BSA) for 20 min and then rinsed and stored in 1X PBS (pH 7.4) solution. 100 µL of samples in 1X PBS (pH 7.4) solution were injected into secondary or tertiary veins via pulled glass capillary needles. Embryo chorioallantoic membrane vasculature was imaged using a customized avian embryo chamber and a Zeiss Axio Examiner upright microscope with a heating stage.

In Vivo Toxicity Studies: All animal procedures complied with the guidelines of the University of New Mexico Institutional Animal Care and Use Committee and were conducted following institutional approval (Protocol 17-200658-HSC). The animal experiments were performed on female Albino C57BL/6 mice (6 weeks) from Charles River Laboratories. To evaluate the in vivo toxicity of armored RBCs, PBS (Control), MSN@ZIF-8 hybrid NPs (1mg NPs per mice), and the related armored RBCs (1mg NPs on armored RBCs per mice) were administered by retro-orbital injections at day 0. At day 28 post-injection, blood was collected with each group contained four mice. Blood cell counts by population and blood metabolites obtained using the Abaxis VetScan System and piccolo metabolite discs. On the same day, all these animals were sacrificed and their liver, lung, kidney, spleen, and heart were collected. Following fixation and paraffin embedding, tissues were stained with H&E, sectioned, and examined for morphological changes.

Pharmacokinetics and Biodistribution Studies: The animal experiments were performed on female Albino C57BL/6 mice (6 weeks). To evaluate the circulation half-life of NPs and armored RBCs, DyLight 800-labeled MSN@ZIF-8 hybrid NPs and the related armored RBCs were used. Briefly, both samples were incubated in 1X PBS (pH 7.4) solution with 10 mg mL^{-1} BSA for 30 min and then rinsed and stored in 1X PBS (pH 7.4) solution. 150 µL of NPs (1mg mL^{-1}) and the related armored RBCs (1 mg mL^{-1} NPs on armored RBCs) were injected into the eye of the mice. The blood was collected at 0.5, 1, 2, 6, 12, and 24 h following the injection. Each time point group contained three mice. The collected blood samples were diluted with the same amount of 1X PBS before the fluorescence measurement. Particle retention in circulation at these time points was determined by measuring the fluorescence on a BioTek microplate reader (Winooski, VT). Pharmacokinetics parameters were calculated to fit a two-compartment model. To study the biodistribution of the NPs and armored RBCs in various tissues, 150 µL of NPs (1 mg mL^{-1}) and the related armored RBCs (1 mg mL^{-1} NPs on armored RBCs) were retro-orbital injected to mice. At 12 and 24 h time points following the particle injection, three mice were randomly selected and euthanized. Their liver, spleen, kidneys, heart, lung, and blood were collected. The collected organs were examined with an IVIS fluorescence imaging system (Xenogen, Alameda, CA), and the fluorescence intensity of the NPs and armored RBCs in different organs was further semi-quantified by the IVIS imaging software.

Supporting Information

Supporting Information is available from the Wiley Online Library or from the author.

Acknowledgements

J.G. and Y.Y. contributed equally to this work. C.J.B. acknowledge support from the University of New Mexico Center for Micro-Engineered Materials. C.J.B. and R.E.S. acknowledge support from NIH RO1 (FP0003261 and CA226537). C.J.B. acknowledges support

by the Sandia National Laboratory Laboratory-Directed Research and Development Program and support from the Department of Energy Office of Science, Division of Materials Science and Engineering. This work was supported, in part, by the National Science Foundation (NSF) under Cooperative Agreement No. EEC-1647722. R.E.S. acknowledges use of the UNM Animal Models and Microscopy facilities, supported by UNM Comprehensive Cancer Center NCI grant 2P30 CA118100-11. W.Z. acknowledges the financial support from National Natural Science Foundation of China (21972047), Guangdong Provincial Pearl River Talents Program (2019QN01Y314), and the Program for Guangdong Introducing Innovative and Entrepreneurial Teams (2019ZT08Y318). E.P. acknowledges funding by the Deutsche Forschungsgemeinschaft (DFG) project PL 696/4-1. S.W. acknowledges funding from the Basque Government Industry Department under the ELKARTEK and HAZITEK programs. An equal contributorship statement was added to the Acknowledgements on March 3, 2021, after initial online publication.

Conflict of Interest

The authors declare no conflict of interest.

Keywords

bioapplications, biohybrid materials, metal-organic frameworks, multifunction, red blood cells

Received: July 14, 2020
Revised: October 22, 2020
Published online: November 4, 2020

[1] J. W. Yoo, D. J. Irvine, D. E. Discher, S. Mitragotri, *Nat. Rev. Drug Discovery* **2011**, *10*, 521.

[2] a) J. Yan, J. Yu, C. Wang, Z. Hu, *Small Methods* **2017**, *1*, 1700270; b) C. H. Villa, A. C. Anselmo, S. Mitragotri, V. Muzykantov, *Adv. Drug Delivery Rev.* **2016**, *106*, 88; c) C. H. Villa, D. C. Pan, S. Zaitsev, D. B. Cines, D. L. Siegel, V. R. Muzykantov, *Ther. Delivery* **2015**, *6*, 795; d) M. Magnani, L. Rossi, *Expert Opin. Drug Delivery* **2014**, *11*, 677; e) C. Wang, X. Sun, L. Cheng, G. Yang, Y. Li, Z. Liu, *Adv. Mater.* **2014**, *26*, 4794.

[3] a) R. Mukthavaram, G. Shi, S. Kersari, D. Simberg, *J. Controlled Release* **2014**, *183*, 146; b) Y. Godfrin, F. Horand, R. Franco, E. Dufour, E. Kosenko, B. E. Bax, A. Banz, O. A. Skorokhod, J. M. Lanao, V. Vitvitsky, *Expert Opin. Biol. Ther.* **2012**, *12*, 127; c) F. Pierigè, S. Serafini, L. Rossi, M. Magnani, *Adv. Drug Delivery Rev.* **2008**, *60*, 286.

[4] a) J. S. Brenner, D. C. Pan, J. W. Myerson, O. A. Marcos-Contreras, C. H. Villa, P. Patel, H. Hekierski, S. Chatterjee, J. Tao, H. Parhiz, *Nat. Commun.* **2018**, *9*, 2684; b) A. C. Anselmo, V. Gupta, B. J. Zern, D. Pan, M. Zakrewsky, V. Muzykantov, S. Mitragotri, *ACS Nano* **2013**, *7*, 11129; c) D. C. Pan, J. W. Myerson, J. S. Brenner, P. N. Patel, A. C. Anselmo, S. Mitragotri, V. Muzykantov, *Sci. Rep.* **2018**, *8*, 1615; d) A. C. Anselmo, S. Kumar, V. Gupta, A. M. Pearce, A. Ragusa, V. Muzykantov, S. Mitragotri, *Biomaterials* **2015**, *68*, 1.

[5] a) S. Mansouri, Y. Merhi, F. M. Winnik, M. Tabrizian, *Biomacromolecules* **2011**, *12*, 585; b) B. Wang, G. Wang, B. Zhao, J. Chen, X. Zhang, R. Tang, *Chem. Sci.* **2014**, *5*, 3463; c) T. Park, J. Y. Kim, H. Cho, H. C. Moon, B. J. Kim, J. H. Park, D. Hong, J. Park, I. S. Choi, *Polymer* **2017**, *9*, 140; d) J. Y. Kim, H. Lee, J. Park, M. H. Kim, H. Cho, W. Youn, S. M. C. Kang, I. S. Choi, *Chem. - Asian J.* **2016**, *11*, 3183; e) J. H. Park, D. Hong, J. Lee, I. S. Choi, *Acc. Chem. Res.* **2016**, *49*, 792.

[6] a) Z. Wu, T. Li, J. Li, W. Gao, T. Xu, C. Christianson, W. Gao, M. Galarnyk, Q. He, L. Zhang, *ACS Nano* **2014**, *8*, 12041; b) H. Wang, M. Pumera, *Chem. Rev.* **2015**, *115*, 8704; c) H. X, W. Chao, Z. Liu, *Bioconjugate Chem.* **2018**, *29*, 852.

[7] J. Shi, L. Kundrat, N. Pishesha, A. Bilate, C. Theile, T. Maruyama, S. K. Dougan, H. L. Ploegh, H. F. Lodish, *Proc. Natl. Acad. Sci. U. S. A.* **2014**, *111*, 10131.

[8] J. H. Park, S. H. Yang, J. Lee, E. H. Ko, D. Hong, I. S. Choi, *Adv. Mater.* **2014**, *26*, 2001.

[9] a) E. H. Furukawa, K. E. Cordova, M. O'Keeffe, O. M. Yaghi, *Science* **2013**, *341*, 1230444; b) M. S. Denny Jr., J. C. Moreton, L. Benz, S. M. Cohen, *Nat. Rev. Mater.* **2016**, *1*, 16078; c) P. Horcajada, R. Gref, T. Baati, P. K. Allan, G. Maurin, P. Couvreur, G. Férey, R. E. Morris, C. Serre, *Chem. Rev.* **2012**, *112*, 1232.

[10] a) T. M. McDonald, J. A. Mason, X. Kong, E. D. Bloch, D. Gygi, A. Dani, V. Crocellà, F. Giordanino, S. O. Odoh, W. S. Drisdell, *Nature* **2015**, *519*, 303; b) N. S. Bobbitt, M. L. Mendonca, A. J. Howarth, T. Islamoglu, J. T. Hupp, O. K. Farha, R. Q. Snurr, *Chem. Soc. Rev.* **2017**, *46*, 3357.

[11] a) H. Kim, S. Yang, S. R. Rao, S. Narayanan, E. A. Kapustin, H. Furukawa, A. S. Umans, O. M. Yaghi, E. N. Wang, *Science* **2017**, *356*, 430; b) M. J. Kalmutzki, C. S. Diercks, O. M. Yaghi, *Adv. Mater.* **2018**, *30*, 1704304.

[12] I. Stassen, N. Burtch, A. Talin, P. Falcaro, M. Allendorf, R. Ameloot, *Chem. Soc. Rev.* **2017**, *46*, 3185.

[13] C. H. Hendon, A. J. Rieth, M. D. Korzyński, M. Dincă, *ACS Cent. Sci.* **2017**, *3*, 554.

[14] a) M. Lismont, L. Dreesen, S. Wuttke, *Adv. Funct. Mater.* **2017**, *27*, 1606314; b) R. Freund, U. Lächelt, T. Gruber, B. Rühle, S. Wuttke, *ACS Nano* **2018**, *12*, 2094; c) W. Zhu, G. Xiang, J. Shang, J. Guo, B. Motevalli, P. Durfee, J. O. Agola, E. N. Coker, C. J. Brinker, *Adv. Funct. Mater.* **2018**, *28*, 1705274.

[15] a) C. Avci, I. Imaz, A. Carné-Sánchez, J. A. Pariente, N. Tasios, J. Pérez-Carvajal, M. I. Alonso, A. Blanco, M. Dijkstra, C. López, D. Maspoch, *Nat. Chem.* **2018**, *10*, 78; b) J. Guo, B. L. Tardy, A. J. Christofferson, Y. Dai, J. J. Richardson, W. Zhu, M. Hu, Y. Ju, J. Cui, R. R. Dagastine, *Nat. Nanotechnol.* **2016**, *11*, 1105; c) W. Zhu, J. Guo, S. Amini, Y. Ju, J. O. Agola, A. Zimpel, J. Shang, A. Noureddine, F. Caruso, S. Wuttke, J. G. Croissant, C. J. Brinker, *Adv. Mater.* **2019**, *31*, 1900545.

[16] O. V. Bondar, D. V. Saifullina, I. I. Shakhmaeva, I. I. Mavlyutova, T. I. Abdullin, *Acta Naturae* **2012**, *4*, 78.

[17] M.d. A. Rahim, S. L. Kristufek, S. Pan, J. J. Richardson, F. Caruso, *Angew. Chem., Int. Ed.* **2018**, *57*, 2.

[18] J. H. Cavka, S. Jakonsen, U. Olsbye, N. Guillou, C. Lamberti, S. Bordiga, K. P. Lillerud, *J. Am. Chem. Soc.* **2008**, *130*, 13850.

[19] P. Horcajada, S. Surblé, C. Serre, D. Hong, Y. Seo, J. Chang, J. Grenèche, I. Margiolaki, G. Férey, *Chem. Commun.* **2007**, *27*, 2820.

[20] a) C. I. Biggs, T. L. Bailey, B. Graham, C. Stubbs, A. Fayter, M. I. Gibson, *Nat. Commun.* **2017**, *8*, 1546; b) W. Zhu, J. Guo, J. O. Agola, J. G. Croissant, Z. Wang, J. Shang, E. Coker, B. Motevalli, A. Zimpel, S. Wuttke, C. J. Brinker, *J. Am. Chem. Soc.* **2019**, *141*, 7789.

[21] a) W. Zhu, J. Guo, Y. Ju, R. E. Serda, J. G. Croissant, J. Shang, E. Coker, J. O. Agola, Q. Zhong, Y. Ping, *Adv. Mater.* **2019**, *31*, 1806774; b) Q. Lei, J. Guo, A. Noureddine, A. Wang, S. Wuttke, C. J. Brinker, W. Zhu, *Adv. Funct. Mater.* **2020**, *30*, 1909539.

[22] J. Guo, J. O. Agola, R. Serda, S. Franco, Q. Lei, L. Wang, J. Minster, J. G. Croissant, K. S. Butler, W. Zhu, C. J. Brinker, *ACS Nano* **2020**, *14*, 7847.

[23] S. Jiang, R. Cheng, X. Wang, T. Xue, Y. Liu, A. Nel, Y. Huang, X. Duan, *Nat. Commun.* **2013**, *4*, 2225.

[24] H. Kojima, M. Hirotani, N. Nakatsubo, K. Kikuchi, Y. Urano, T. Higuchi, Y. Hirata, T. Nagano, *Anal. Chem.* **2001**, *73*, 1967.

[25] X. Liu, Q. Yan, K. L. Baskerville, J. L. Zweier, *J. Biol. Chem.* **2007**, *282*, 8831.

[26] Z. Lou, P. Li, K. Han, *Acc. Chem. Res.* **2015**, *48*, 1358.